Temperature measurements of the gas-phase during surrogate diesel injection using two-color toluene LIF

R. P. C. Zegers · M. Yu · C. Bekdemir ·
N. J. Dam · C. C. M. Luijten · L. P. H. de Goey

Abstract Planar laser-induced fluorescence (LIF) of toluene has been applied in an optical engine and a high-pressure cell, to determine temperatures of fuel sprays and in-cylinder vapors. The method relies on a redshift of the toluene LIF emission spectrum with increasing temperature. Toluene fluorescence is recorded simultaneously in two disjunct wavelength bands by a two-camera setup. After calibration, the pixel-by-pixel LIF signal ratio is a proxy for the local temperature. A detailed measurement procedure is presented to minimize measurement inaccuracies and to improve precision. n-Heptane is used as the base fuel and 10 % of toluene is added as a tracer. The toluene LIF method is capable of measuring temperatures up to 700 K; above that the signal becomes too weak. The precision of the spray temperature measurements is 4 % and the spatial resolution 1.3 mm. We pay particular attention to the construction of the calibration curve that is required to translate LIF signal ratios into temperature, and to possible limitations in the portability of this curve between different setups. The engine results are compared to those obtained in a constant-volume high-pressure cell, and the fuel spray results obtained in the high-pressure cell are also compared to LES simulations. We find that the hot ambient gas entrained by the head vortex gives rise to a hot zone on the spray axis.

R. P. C. Zegers, M. Yu contributed equally to this work.

R. P. C. Zegers · M. Yu · C. Bekdemir ·
N. J. Dam (✉) · C. C. M. Luijten · L. P. H. de Goey
Department of Mechanical Engineering, Section Combustion
Technology, Eindhoven University of Technology, Den Dolech
2, 5612 AZ Eindhoven, The Netherlands
e-mail: n.j.dam@tue.nl

R. P. C. Zegers
e-mail: ronzegers@gmail.com

1 Introduction

Accurate non-intrusive 2D temperature measurements under high-temperature conditions as prevalent in internal combustion (IC) engines have been a challenge over the last decade. Mass-averaged temperatures in engines can be derived quite accurately from the in-cylinder pressure evolution. However, temperature stratification resulting from injection of fuel into a cylinder filled with hot air cannot yet be measured accurately. Recent research suggests that toluene laser-induced fluorescence (LIF) is an appropriate measurement technique for measuring gas and vapor temperatures [1–3].

Although the fundamental principle behind the method (the cause of the redshift in the fluorescence spectrum with increasing temperature) does not seem to be well known, this is not a serious limitation for its practical application. Previous work of Koban et al. [4] has shown that (at atmospheric pressure) the fluorescence spectrum does not depend significantly on excitation wavelength (266 or 248 nm), which implies that internal relaxation is sufficiently fast to render the emitting state independent of the actual excited state. In its turn, this implies that the method will not be sensitive to its environment.

The principle of the technique is as follows. After excitation of toluene vapor by means of UV light (248 nm in our case), it emits fluorescence, the spectral distribution of which depends on temperature. After calibration, the ratio of integrated fluorescence intensities in two disjunct wavelength bands provides a convenient measure for the local temperature. As with all ratio-based methods, this technique has the advantage that it is independent of the local excitation laser intensity and toluene density. A potential disadvantage, however, is that the calibration factor does not need to be constant over the whole field of view.

Toluene has a few advantages over other tracers: it has a high fluorescence quantum yield, a relatively large red shift as function of temperature and a lower toxicity than, e.g., benzene [2, 5]. A major disadvantage of toluene LIF is the decrease of its effective fluorescence lifetime with increasing temperature [6]. This is a result of fast depopulation of the excited state due to intersystem crossing (ISC) [7]. Even with high excitation laser fluence, signal level will decrease to noise levels at high temperatures (~700 K in our case) and therefore decrease the precision.

The applicability of the toluene LIF technique in an engine environment was investigated by only a few researchers. Luong et al. [8] measured in-cylinder temperatures without fuel injection. Mannekutla et al. [9] showed the potential of the technique for fuel sprays, but results were tentative, probably due to fuel fluorescence or fuel decomposition in air. In our research, toluene LIF is used as a tool to measure temperatures during and after injection of fuel inside an optically accessible heavy-duty engine and a constant-volume high-pressure cell. Toluene LIF is used because of the promising outlook of the technique and its relatively modest equipment requirements.

Temperature stratification after spray injection is of major importance for partially premixed combustion (PPC) strategies in diesel engines. In the PPC regime, there is a finite time delay between end of injection and start of combustion, resulting in premixed fuel and air regions with various temperatures and fuel concentrations. Earlier toluene LIF studies have not aimed at measuring temperature stratification after fuel injection.

Cycle-to-cycle variations influence the mixture formation and therefore the time and location where combustion starts. Controlling the ignition event is a major research topic in the application of PPC combustion strategies in practical combustion engines. For this reason, we investigate the mixture properties by means of planar (2D) toluene LIF on the basis of single laser shots. The use of

toluene LIF has the advantage that the toluene itself serves as a fuel tracer, whereas the redshift of its fluorescence is a temperature marker (for the vapor phase). To better interpret the data from the optical diesel engine, we compare those results with measurements on a single fuel spray in a constant-volume high-pressure cell with more extensive optical access, which in turn are compared with LES simulations.

2 Materials and setup

In this research, two setups are used: an optically accessible one-cylinder engine and a constant-volume high-pressure cell (HPC).

2.1 Optically accessible engine

The engine setup consists of a one-cylinder optically accessible heavy-duty diesel engine, based on a Ricardo Proteus block and equipped with a DAF MX cylinder head. The engine is driven by an electrical motor. A schematic layout of the complete setup is given in Fig. 1 and a cross section of the engine is shown in Fig. 2. The piston is elongated, and the upper part of the liner and the piston bottom are both made of sapphire. Via an oval aluminium-coated mirror (Molenaar Optics), positioned under 45°, optical access to the combustion chamber is obtained. The hydraulic cylinder can be lowered, allowing easy access to the combustion chamber for cleaning. For details of the engine, we refer to [10]. Specifications are summarized in Table 1.

The engine is equipped with both a port fuel injection (PFI) system (used for toluene injection in the intake manifold) and a common rail injector of Delphi Diesel Systems (used for fuel injection). The fuel is pressurized with a commercially available air-driven pump from

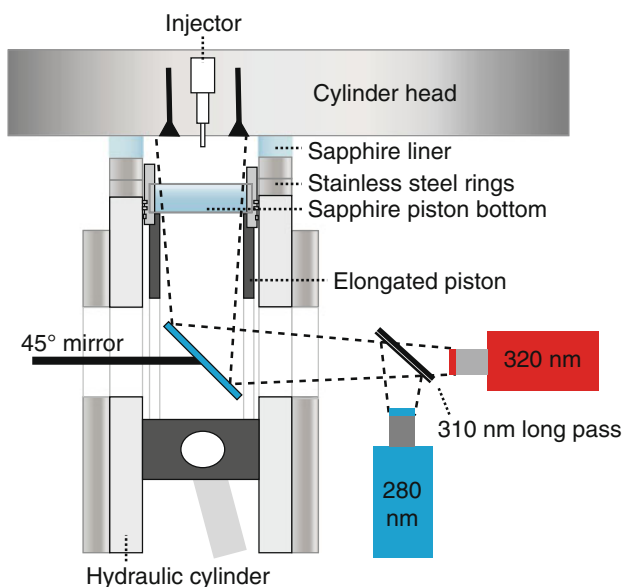**Fig. 1** Schematic layout of the optical engine setup
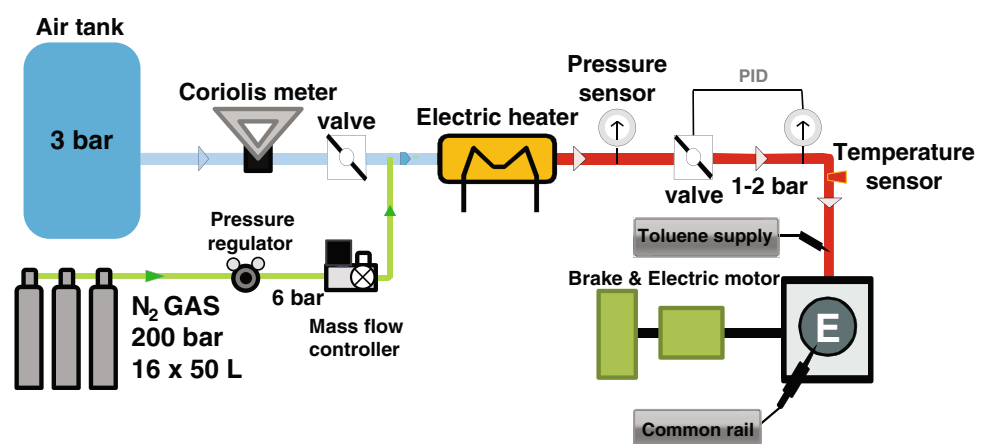
Fig. 2 Cross section of the optically accessible engine

Table 1 Engine specifications, top dead center (TDC) is defined as 360 CAD (crank angle degrees)

Bore	130 mm
Stroke	156 mm
Connecting rod	270 mm
Displacement volume	2.07 l
Compression ratio	13.9
IVO	715 CAD
IVC	190 CAD
EVO	500 CAD
EVC	10 CAD
Piston bowl/crown	Flat bathtub
Piston bowl diameter	90 mm
Piston bowl depth	20 mm

IVO inlet valve opening, *IVC* inlet valve closing, *EVO* exhaust valve opening, *EVC* exhaust valve closing

Resato and the total fuel line has a volume of approximately 500 ml. Toluene is pressurized in a 100-ml vessel using compressed nitrogen at 4 bar and is directly connected to two PFI injectors which are controlled by a MOTEC M8 programmable motor management system. The distance between the PFI injectors and the inlet valve is approximately 50 cm. The details of the common rail diesel injector are presented in Table 2.

2.2 High-pressure cell

The HPC is essentially a constant-volume combustion vessel dedicated to optical diagnostics on single fuel

Table 2 Fuel injector specifications

Holes	7
Hole size	195 μm
Flow (nominal)	1.7 l/min
Spray cone angle (ϕ)	143°

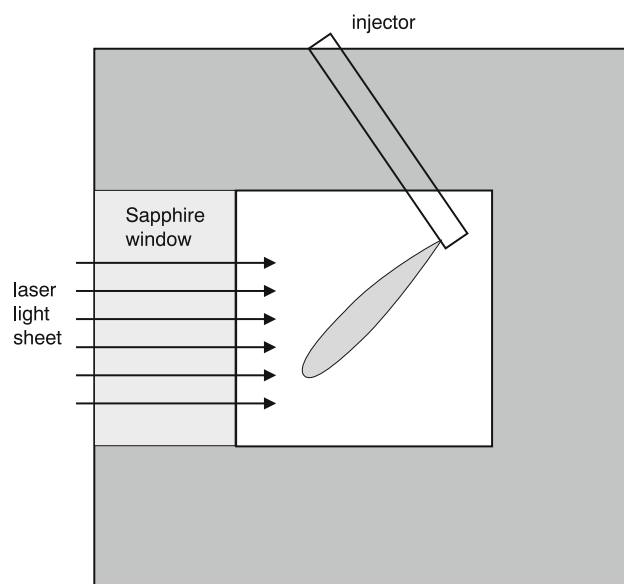Nominal flow as measured by Delphi Diesel Systems at 100 bar (without needle)

Fig. 3 Schematic vertical cross section of the HPC, through the plane of fuel injection. Two more windows are at the front and back side of the cell, along a line perpendicular to the laser light sheet. The whole cell can be heated, and there is an internal fan to improve mixing

sprays. Its core is a cubic 1.26 l combustion chamber produced by spark erosion inside a stainless steel cube. It is equipped with subsystems for heating, cooling, fuel injection, gas supply, computer control, data acquisition and optical diagnostics. Three sides provide optical access through large sapphire windows. A single fuel spray can be injected along a diagonal in a vertical plane (see schematic view in Fig. 3). Ambient conditions are created by means of the so-called pre-combustion technique: a combustible mixture of specifically tailored pressure and composition is ignited (the pre-combustion), which raises temperature and pressure in the HPC. The fuel spray is injected when the cell contents have cooled down to the desired conditions. The composition of the end gas of the pre-combustion determines whether the fuel spray is injected into an inert (no O_2 left) or oxidative (O_2 left) environment. A more detailed description of the HPC is provided by Baert et al. [11]; its main features are summarized in Table 3.

The gas supply system is based on four mass flow controllers, which enable filling pure gases one by one to prepare the gas mixture inside the HPC. The filling process

Table 3 Specifications of the HPC

Basic parameters	
Shape of the chamber	$108 \times 108 \times 108$ mm^3 (1.26 l)
Window size	50 mm thick, 100 mm diameter
Maximum pressure	300 bar (sapphire windows)
Heating and cooling system	
Wall temperature	293–473 K
Fuel temperature	313–423 K
Injector holder temperature	333 K
Fuel supply system	
Injector	Delphi single hole nozzle
Injector coating	TiN coated
Nozzle hole size	150 μm
C_d	0.86 (at 800 bar)
C_m	0.77 (at 800 bar)
Sensors	
Gas pressure	Druck PMP 4070 (0–70 bar)
Injection pressure	Kistler 4067A5000 (0–5,000 bar)
Pre-combustion pressure	Kistler 6041 AU20 (0–250 bar)

Table 4 The components of the toluene LIF setups

Laser	Lambda Physik, Compex 350T
Laser wavelength	248 nm
Toluene	Sigma Aldrich HPLC grade 99.6 % pure
Dichroic beam splitter	310 nm long pass
	Semrock FF310-Di01
Bandpass filter 1	320 nm FWHM 43.8 nm
	Semrock BrightLine FF01-220/40
Bandpass filter 2	280 nm FWHM 22 nm
	Semrock BrightLine FF01-280/20
Lenses	Halle OUC 2.5, $f = 100$ mm, F# = 2
ICCD camera 1	Princeton instruments PI-MAX 3
ICCD camera 2	Princeton instruments PI-MAX 3
ICCD camera 3	Princeton instruments PI-MAX 2
ICCD photocathode coating	Unigen II
Camera resolution	16 bit

is monitored by the gas pressure sensor. A mixing fan is used to enhance the mixing. We use C_2H_2, O_2, N_2 and Ar to form a mixture, which, once burned, produces the same density, O_2 mass fraction and heat capacity as those expected at the desired engine condition.

2.3 LIF setup

Each toluene LIF setup contains two cameras which are used in various configurations, as described in the sections below. The specifications of the equipment are similar for all configurations.

2.3.1 General specifications

The components used in the toluene LIF setups are specified in Table 4. Both bandpass filters have a diameter of 50 mm to fit the UV lenses. Due to the failure of camera 2, three different cameras have been used. These have been named camera 1 to 3. The transmission efficiencies of the used filters, lenses, sapphire windows and the dichroic beam splitter, as well as the reflection efficiencies of the aluminium-coated mirror and the quantum efficiency of the photocathode of the cameras over the wavelength range of interest are plotted in Fig. 4.

2.3.2 Illumination

For all experiments, we use a light sheet derived from a broad-band KrF excimer laser (Lambda Physik Compex 350; nominal $\lambda = 248$ nm). In the HPC, the laser light
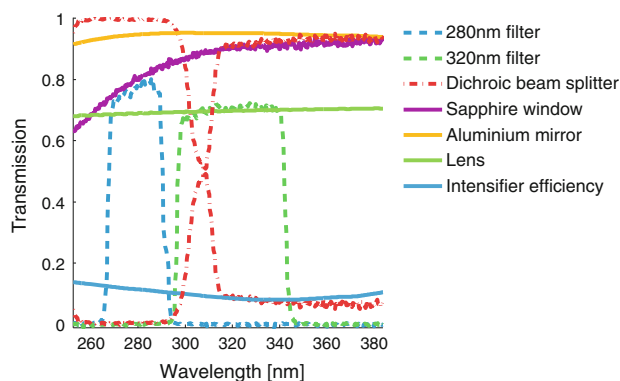
Fig. 4 Transmission efficiencies, reflection efficiencies and photocathode quantum efficiency (QE) of the optical detection line. All values are based on manufacturer specifications
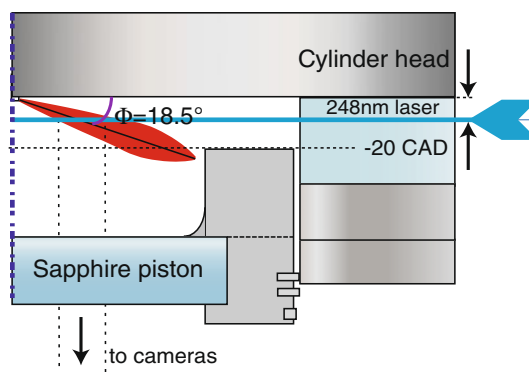
Fig. 5 Spray image schematic in the optical engine, with the laser sheet in *blue* and the spray in *red*. The cone angle of the injector is 143°

sheet contains the spray axis. In the optical engine, this was not possible. Here, the horizontal light sheet enters the combustion chamber 5 mm below the cylinder head

(Fig. 5). Its thickness varies between about 1 and 2 mm throughout the combustion chamber. Therefore, only a relatively small cross section of the fuel sprays is illuminated directly. However, in the actual measurements, the apparent cross sections may be larger due to illumination by scattered laser light.

2.3.3 Camera configuration

The toluene LIF thermometry technique requires two images to be taken from the same event in two different wavelength ranges. The latter are indicated by the two boxes in the LIF spectra of Fig. 6. Acquiring these two
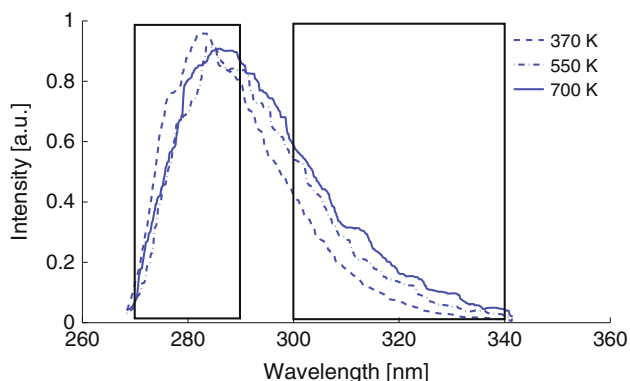

Fig. 6 Normalized toluene LIF spectrum at three different temperatures. The *two boxes* indicate the wavelength regions of the bandpass filters
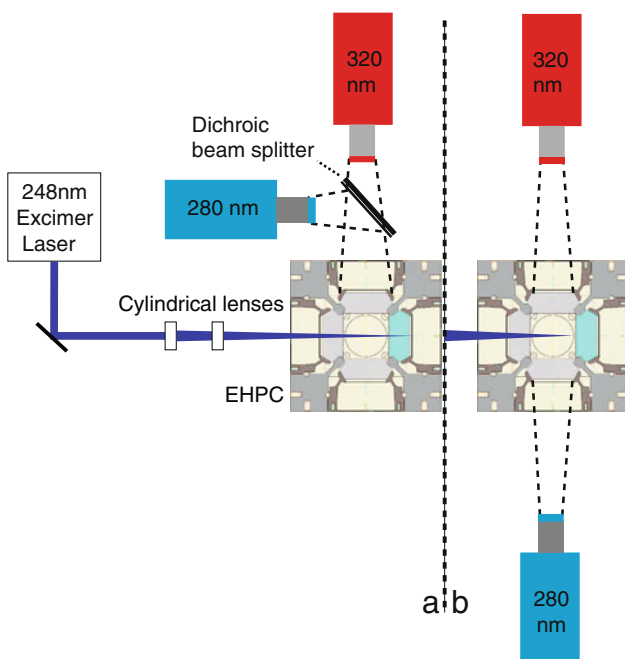

Fig. 7 Schematic view of both camera configurations in the HPC setup. **a** Same side setup, **b** opposite side setup

images can be done either by one single camera or by two separate ones. The former has the advantage of minimized cost, but goes at the expense of spatial resolution and somewhat complicated measures for image separation (see, e.g., [12]). The latter is more flexible, and is the method chosen here. In both cases, the individual images have to be mapped onto each other and corrected for pixel-to-pixel variations in sensitivity.

When using two cameras, they can be positioned on opposite sides or on the same side of the measurement volume; in the latter case, a beam splitter can be used to separate the spectral bands. The two strategies are shown in Fig. 7 for the HPC setup. A same side camera configuration requires only one path for optical access. A disadvantage of the same side camera configuration is the requirement of a (dichroic) beam splitter to split the signal into two parts or two wavelength ranges. A regular beam splitter will transmit or reflect a part of the total signal only, which reduces the sensitivity. A dichroic beam splitter will in theory reflect and transmit the wavelengths of interest but needs to be positioned precisely to avoid a difference in wavelength reflection. An opposite side camera configuration on the other hand avoids the use of the dichroic beam splitter, and the cameras can be positioned closer to the setup. A drawback of the opposite site arrangement is the difference in line-of-sight of both cameras. Since both pre-combustion and the spray penetration involve strong turbulence, the difference in light path may induce distortion in the images, decreasing the spatial resolution. A two-side camera configuration has been used previously in [3, 13] and did not reveal any major drawbacks.

For the experiments on the optical engine, a same side configuration is the only option. On the HPC, however, both options are possible. Here, we have tested both approaches, using a dichroic (rather than a broad-band) beam splitter to split the fluorescence immediately into the desired wavelength ranges. As it happens, the optical characteristics of the dichroic beam splitter are sensitive to the angle of incidence of the light, which may vary over the field of view if the object is not at infinity. The implications of this effect for the temperature calibration will be discussed further below (Sect. 5.2).

3 Aspects of quantitative measurements

To perform accurate toluene LIF measurements, special attention has to be paid to several aspects concerning the equipment and measurement procedure. In particular, the potentially most serious pitfall of allegedly spectrally resolved measurements through spectral bandpass filters, rather than a spectrograph, is that the information of the spectrum is in fact lost. The interpretation of the light

intensity measured behind the bandpass filters necessarily relies on the assumption that the underlying spectrum has not been compromised. (This complication, of course, pertains to measurements through bandpass filters in general, not just to the present toluene LIF measurements.) Various aspects will be systematically described and discussed in the following subsections. Data processing steps are given in Appendix B.

3.1 Fuel

The base fuel should not contain any species, other than the tracer, which fluoresce in the wavelength range of interest upon illumination at 248 nm. Therefore, HPLC grade toluene and n-heptane base fuel were used.

Figure 8 shows an example of fluorescence images after the injection of a pure n-heptane spray in the HPC into

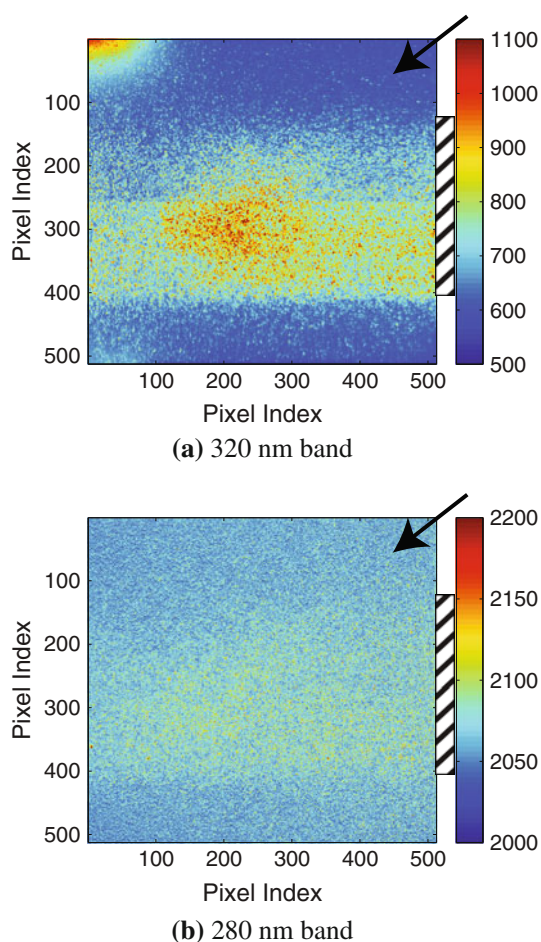
(a) 320 nm band

(b) 280 nm band

Fig. 8 Raw LIF images of pure n-heptane injection in the HPC into residual pre-combustion gas at about 600 K. The fuel is injected outside the *top right corner* (*arrow*). The increased signal in the center of the 320 nm image originates from fluorescent impurities in the fuel. The *top left corner* of the 320 nm signal shows increased signal due to a small light leak. Hatching indicates the extent of the laser light sheet

residual pre-combustion gas at about 600 K, recorded with the opposite side camera configuration. In the 280 nm range, the spray is barely visible. However, in the 320 nm wavelength band, the spray increases the signal with about 150 counts above the residual gas intensity, presumably due to fluorescent impurities in the fuel. The residual gas itself, without fuel injection, does not show any detectable fluorescence in both wavelength bands. Previous research also mentions background signal from impurities, but neglected it because the signal levels were below 10 % of the toluene signal [3]. However, the increased background level is not constant over the field of view and needs to be recognized when evaluating the results.

3.2 Tracer

Even in the absence of oxygen, the tracer lifetime may be limited due to thermal decomposition. In the optical engine, the tracer is injected into the inlet gas, way before fuel injection. In the HPC, this is not possible, since the toluene would not survive pre-combustion; therefore, toluene is mixed into the fuel that is injected into the HPC. The residence time (before laser excitation) at high temperature is in both cases much less than about 0.1 s, so that thermal decomposition is not expected to be significant [4]. At high tracer density, the excitation laser beam will be absorbed on its way through the combustion chamber. This should not affect the fluorescence ratios (more on this below), but does of course limit the signal strength away from the entrance window of the laser beam. The toluene concentration must be adjusted to an acceptable compromise between signal level and signal uniformity. Fluorescence trapping might play a role in our experiments, in spite of the redshift of the toluene fluorescence relative to its absorption spectrum [2]. The absorption spectra of toluene [4] extend to 290 nm at temperatures around 700 K; therefore, different toluene concentrations from those used during calibration might influence the amount of fluorescence trapping.

3.3 Laser

The laser energy may vary from shot to shot, but the normalized fluorescence spectrum does not change with laser power.

The magnitude of the laser fluence [mJ/cm^2] does affect the fluorescence yield. At low fluence, the fluorescence yield rises linearly with laser pulse energy, but at higher fluence, saturation sets in and the fluorescence yield levels off. Eventually, under conditions of full saturation, the fluorescence yield is independent of laser pulse energy. Although it is generally advised to stay away from saturation [3], it is not immediately obvious why the LIF ratio
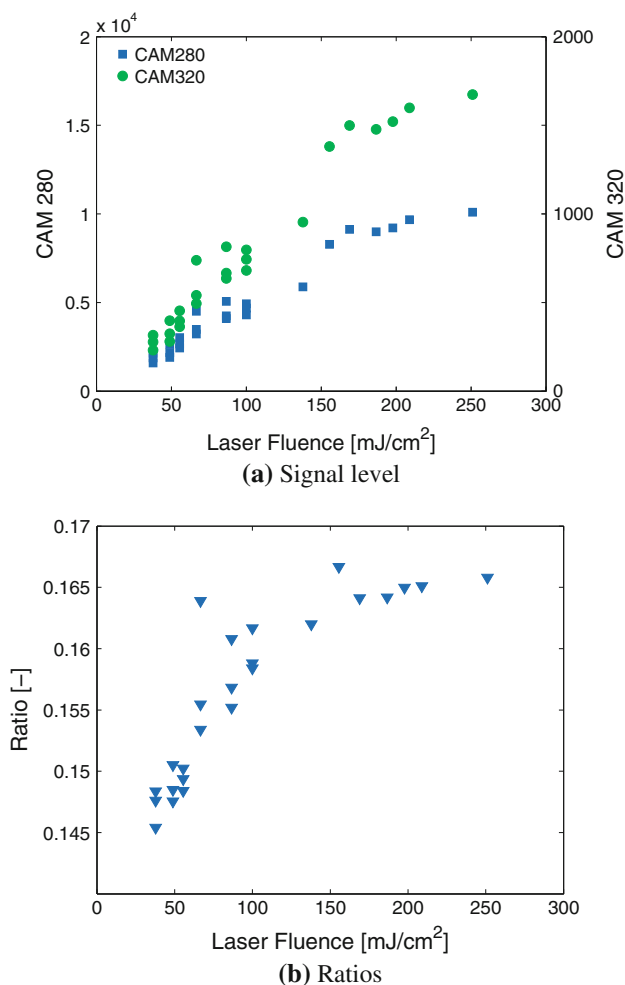
(a) Signal level

(b) Ratios

Fig. 9 LIF intensities and ratios as a function of (single shot) laser fluence obtained in the optically accessible engine at 300 CAD, with an inlet air temperature of 50 °C. The 320/280 ratios represent a temperature span of approximately 460 ± 15 K

method would not work any more when the fluorescence yield is saturated.

To delimit the linear regime, we recorded the bandpass-filtered LIF signals of toluene vapor at a fixed CAD and inlet temperature in the motored optical engine, and calculated the ratio of the signals on the two cameras. The laser fluence, relative to the beam waist of 1.5 mm and assuming negligible absorption, was varied from approximately 50 to 250 mJ/cm^2 with constant toluene concentration and camera gain. The measured average pixel values are shown in Fig. 9a as a function of laser fluence. When looking at the calculated 320/280 ratio (Fig. 9b), it can be concluded that increasing the laser fluence above 150 mJ/cm^2 does not influence the ratio. Remarkably, the ratio does change for a laser fluence below 150 mJ/cm^2. This is explained by the low overall signal levels (hence lower signal-to-noise) on the 320 nm camera. Other researchers mention a laser fluence of about 50 mJ/cm^2 as

the upper limit for linear fluorescence response [3], which contradicts with our findings. Currently, the results published on the assumed ratio change as a function of fluorescence saturation are inconclusive. Therefore, all experiments presented below are conducted with moderate laser power levels around 150 mJ/cm^2 just before entering the engine.

3.4 Camera

The quantum efficiency of the intensifier photocathode is dependent on the incoming wavelength. In the wavelength region around 300 nm, the quantum efficiency of the Unigen II coating of our camera systems (originally purchased for experiments around 200 nm) is in the order of only 10 %. We compensate for this relatively low efficiency by using a 2×2 pixel binning approach, resulting in a decreased spatial resolution of 512×512 pixels.[1]

ICCD cameras only respond linearly to the incoming amount of photons over a certain intensity range. Also multi-channel-plate (MCP) saturation needs to be avoided [14]. To check the linearity range, the camera signal level as function of the incoming light intensity from a diffusive screen illuminated by white light is measured and the light intensity is adjusted by means of the camera lens diaphragm. The observed maximum intensity of the linear range is different for all cameras used and is 1.2×10^4 counts for camera 1, 2.5×10^4 counts for camera 2 and 6.0×10^4 counts for camera 3 (on a full dynamic scale of 6.5×10^4). It should be mentioned that this test was performed with a white light source and the MCP might now saturate earlier than for the UV wavelengths. In the experiments, signal levels stayed below the saturation onsets indicated above.

3.5 Dichroic filters and the finite solid angle of light collection

The characteristics of multi-layer coated beam splitters and narrow bandpass filters depend on the angle of incidence of the incident light. In a first-order approximation, the variation of cut-off wavelength with angle of incidence θ_i can be described by

$$\lambda(\theta_i) = \lambda_0 \sqrt{1 - \sin^2 \theta_i / n_{\text{eff}}^2} ,$$

in which the effective refractive index n_{eff} depends on the filter, and λ_0 is the filter design wavelength at normal incidence. The shift is always to the blue, and can amount to a few percent of the design wavelength for moderate angles of incidence. Specific data can be found on

---

[1] Note that intensifiers with higher efficiencies (around 25 %) are commercially available.
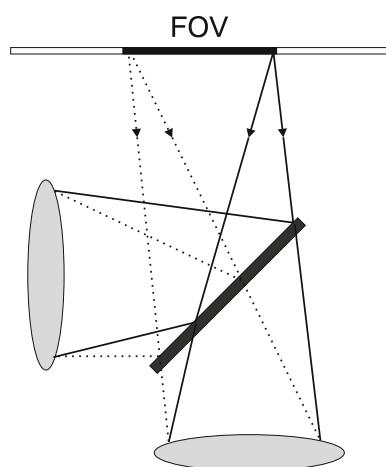
Fig. 10 Schematic representation of the angle of incidence variation over the FOV. The *gray ellipses* indicate the camera lenses

manufacturers web sites; see e.g., [15]. In light-starved applications like ours, the desire to harvest as much light as possible naturally leads to the use of fast collection optics close to the source. This, however, implies both an angle of incidence variation over the field of view and over the solid angle that contributes to single pixels. The situation for the 45° beam splitter is schematically illustrated in Fig. 10.

For the HPC measurements, the distance between the HPC and cameras is reduced as much as possible, and this was found to cause a gradient in the temperature calibration over the field of view (same side setup only). We discuss our approach to correct for that in Sect. 5.2 of this paper.

3.6 Collisional quenching

Previous research shows a large influence of molecular oxygen on the fluorescent signal by collisional quenching, the efficiency of which changes as function of temperature [6, 16]. To achieve the highest possible signal and to avoid oxidation of the fuel, all experiments have been conducted without oxygen.

3.7 Background subtraction

In all experiments, the recorded fluorescent images also contain background consisting of several contributions. Part of the background concerns hardware offset (fixed) and dark current (depends on settings). However, the background in the HPC also contains fluorescence from pre-combustion residual gas, and during spray injection also fluorescence of the fuel, as shown in Fig. 8. To correct for the background fluorescence level of pre-combustion residual gas, the image recorded 0.2 s (5 Hz recording speed) prior to the spray image is used as background and subtracted pixel by pixel from the spray measurement. The

influence of the decreasing temperature between the background recording and the spray, which is in the order of 10 K, is neglected. The shot-to-shot fluctuations of laser power introduce fluctuations in the background signal, however, the additional error is less than 1 % of the total signal. The background signal from the base fuel is difficult to remove because the temperature response of the fluorescence signal is unknown. This contribution increases the intensity of the 320 nm image by 2–7 %, depending on the operating conditions, in both the engine and HPC measurements.

3.8 Spatial alignment

Spatial alignment is performed by recording a grid image with both cameras. Using a linear conformal transformation, distortions due to translation, rotation and scaling are accounted for. After transformation, the grid lines in both images match each other with a precision corresponding to the 2 pixel thickness of the grid lines.

3.9 Flat-fielding

The response of an ICCD camera-based detection system cannot be expected to be uniform over the CCD chip. Contributions to the non-uniformity may arise from individual pixel sensitivity variations, non-uniform amplification in the image intensifier, local variations in the photocathode quantum efficiency, vignetting by collection optics and spatial variations in the spectral characteristics of the filters used (see Sect. 3.5 above). Insofar as the response is linear, the net non-uniformity can be corrected for by means of the so-called flat-field image: an image recorded by the detection system of a uniformly lit object plane. Non-uniformities in the flat-field image are the net result of non-uniformities in the whole detection chain: essentially, the pixel values in the flat-field image (after
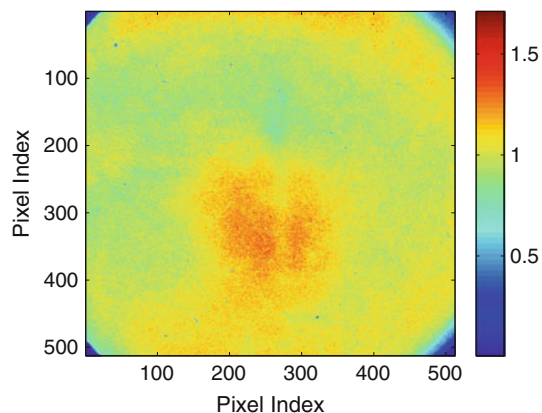

Fig. 11 Image of a uniformly lit plane recorded with defocused camera lens; camera 1 with Halle lens. Pixel values in arbitrary units

background subtraction) can be treated as individual scale factors. The flat-fielding method corrects for sensitivity variations across the photocathode, phosphor screen and CCD chip. When the flat-field image is determined with a lens mounted on the camera, lens abberations and vignetting are also accounted for [14, 17]. Accurate flat-fields for both cameras are the key to achieve accurate image ratios and minimize systematic error.

Flat-field images were recorded with defocused camera lenses from a diffusely reflecting screen illuminated by a white light source. To account for possible wavelength dependence in the flat-field images, a UV light source in the spectral range of the toluene fluorescence is preferred. Figure 11 displays the flat-field image of camera 1; it shows a difference in sensitivity between pixels of approximately a factor of 2 over the whole field of view. A vignetting effect in the corners is also clearly seen, although in this case that is largely due to a mismatch between the square CCD array and the circular image intensifier, and cannot be corrected for. In the opposite camera configuration, a modified flat-fielding method without bandpass filters is used, as previously used by Tea

et al. [3], to quantify the relative sensitivity difference between the two cameras. We will call this "relative flat-fielding" below, because it boils down to comparing corresponding pixel sensitivities on two camera's to each other. Using fluorescence induced by illuminating the HPC filled with toluene vapor and N_2 by a thin light sheet, the camera sensitivities are compared for the UV wavelength bands used for the actual measurement. Again, relative pixel-to-pixel sensitivity variations in the region of interest vary by approximately a factor of 2.

Note that the relative flat-fielding technique has the potential disadvantage of unequal optical paths to the two cameras involved. This will not be an issue in the flat-fielding itself, for which the HPC contains only N_2 and toluene vapor, but may become a concern during measurements on a potentially dense spray.

3.10 Evaluation of spatial alignment and flat-field correction

The purpose of spatial alignment and flat-field correction is to force the two cameras to show the same response to the

Fig. 12 Signal intensity correlation for an image pair obtained in one side (*left column*) and opposite configuration (*right column*). **a**, **b** Original; **c**, **d** after spatial alignment; **e**, **f** after relative flat-fielding correction. The one-side images are obtained by using a 30–70 % beam splitter. The used images are 12 × 12 pixel neighbor average filtered, and background is subtracted

(a) Original one-side

(b) Original opposite-side

(c) Spatial alignment

(d) Spatial alignment

(e) relative flat-field correction

(f) relative flat-field correction
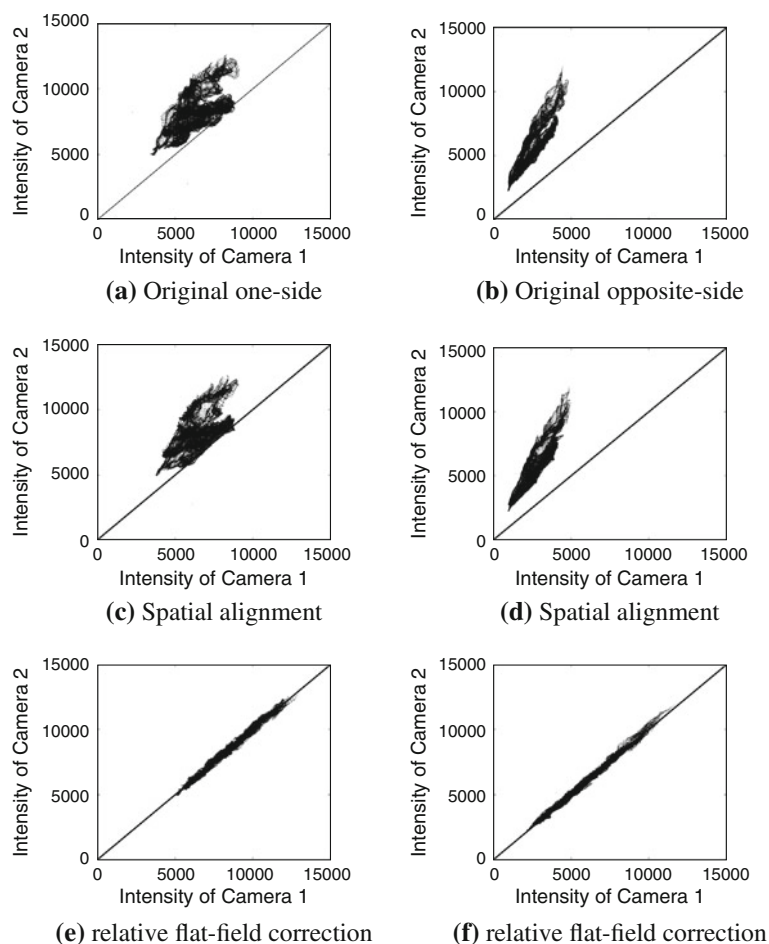
same fluorescent signal, so as not to introduce errors in the fluorescence ratio calculation.

Figure 12 shows a number of image intensity correlation graphs. The location of each data point in the graphs is determined by the corresponding pixel values on two cameras, in the same side configuration (left column) and in the opposite side one (right column). Both cameras looked at the same scene: HPC filled with toluene vapor and N$_2$. For the same side configuration, a 30/70 broadband beam splitter was used, in order to really have both cameras looking at the same source. Figure 12a and b shows the raw data, in which the cameras have been aligned mechanically only, but the signals have not been processed other than by background subtraction and 12×12 nearest-neighbor averaging. Obviously, both cameras respond differently, and the cloud of data points is broad and far removed from the 'ideal line' of equal pixel intensities. Improved alignment in software produces the middle row of Fig. 11, but this does not show much of an improvement. Flat-fielding, in this case using relative flat-fielding based on the average of ten separate images recorded by both cameras, brings a major improvement, as shown in the lower row of Fig. 11. The residual standard deviation of the pixel value ratios amounts to 2 % for the same side and to 3 % for the opposite side configuration.

4 Calibration

Calibrating the LIF ratio versus temperature relation is a tedious but crucial task. The most direct calibration procedure, at least in principle, would be to determine this ratio for toluene at a known range of temperatures, using exactly the same setup as would be used in the actual experiments. To avoid the need to perform such a calibration each time the optical setup is changed, or for cases in which the ideal calibration procedure is not practically feasible, we here use an alternative approach. This approach is based on the notion that the *emitted* spectrum is characteristic for toluene (independent of the environment), but that the *measured* spectrum will be different because of all optics in between the emission and the detector. If we start out with accurate *emitted* spectra over a range of temperatures, and know the optical characteristics of all elements in the detection path, then the spectrum that would be measured at any temperature in a particular setup can be reconstructed, and the LIF ratio calculated. This procedure will be detailed below. We use temperature-dependent spectra recorded at IFPEN as a basis [1], and in the end compare temperatures derived from LIF ratios with global temperatures in our optical engine.
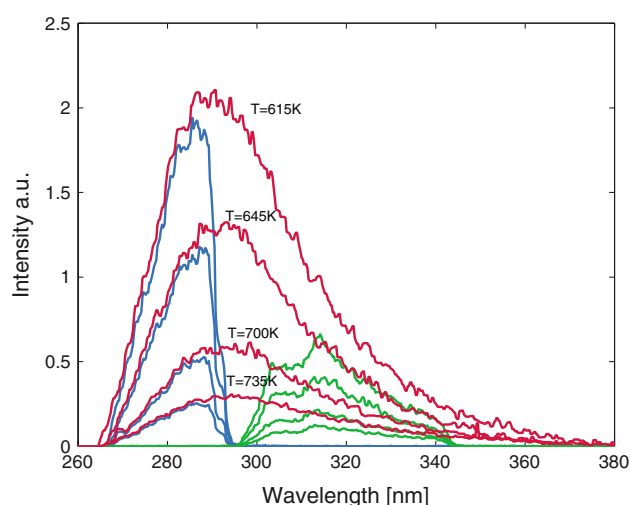

Fig. 13 Measured toluene spectra (*red*) from IFPEN for different temperatures multiplied with the transmission and reflection efficiencies from Fig. 4. The resulting 280 nm part of the spectrum is *blue* and the 320 nm part is *green*

4.1 Optical path corrections

The correction for the optical path consists of two steps: (1) the IFPEN base data were transformed into emission spectra by correcting for the wavelength dependence in the IFPEN spectrometer by Tea et al. [3]; (2) the resulting emission spectra are transformed into spectra that we would measure in our setups. From these spectra and the filter characteristics, the LIF ratios for our setups are calculated as a function of temperature. The optical path corrections of step (2) include the wavelength-dependent transmission/reflection coefficients of camera lenses, the sapphire piston window, mirrors (incl. the dichroic beam splitter in the case of the same side setup), and the photocathode of the ICCD cameras used; these were given in Fig. 4. As an example, the emission spectra reconstructed from the IFPEN data for various temperatures (red) are shown in Fig. 13, together with the spectra arriving at our ICCD cameras after reflection or transmission by the dichroic mirror (setup of Fig. 7a). Obviously, the transition region in the transmission/reflection characteristics of the dichroic mirror significantly reduces spectral intensity in the 300 nm region.

For this calibration approach, different overall camera sensitivities ("overall" meaning apart from flat-field corrections that have been discussed above) have to be taken into account explicitly. We determine the relative sensitivity in a straightforward way, by recording images from the same object under constant illumination. This factor varies with gate time, camera gain and recording speed, and has been determined separately for each measurement condition.
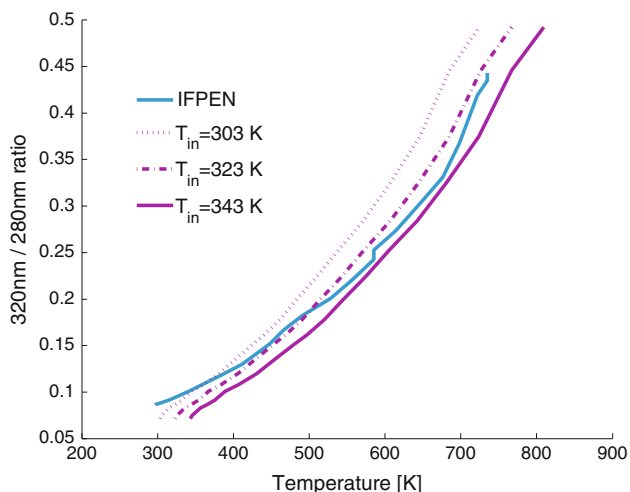
Fig. 14 Temperature calibration lines from the optical engine in Eindhoven and at IFPEN. The *red curves* are based on the same LIF data but with three different assumptions for the IVC temperature

4.2 Engine model

A multi-zone engine model, which incorporates a Woschni correlation to estimate the heat loss to the cylinder walls [18], is used to calculate the bulk in-cylinder temperature. Our model does not account for blow-by losses via the piston rings, and the bulk in-cylinder temperature at the moment of intake valve closing (IVC in Table 1) is treated as a variable, ranging between 30 and 70 °C. Figure 14 shows the LIF ratio versus temperature plots derived in this way for various IVC temperatures and compares them to the similar data derived from the original IFPEN curves, corrected for the differences in the optical setup used in both experiments, as described in the previous section. Clearly, the curves are very similar, but the IFPEN data cross several of our curves for different IVC temperatures. This may be due to differences in the IFPEN temperatures that are derived from the in-cylinder pressure trace and also include an unknown inaccuracy.

4.3 Uncertainty analysis

We estimate the precision, or random error, in the final result starting from the flat-field-corrected images discussed in the context of Fig. 11. The standard deviation of pixel values around the 'ideal line' amounts to 2 and 3 % for the same side and opposite side configurations, respectively. Thus, the standard deviation in the LIF ratio amounts to about 4 %. Depending on the actual value of the ratio (see Fig. 14), this translates into a temperature precision of 7–12 K for ratios between 0.1 and 0.4.

The accuracy, defined here as the uncertainty due to systematic errors in the procedure, originates from several sources: undesired fluorescence from the base fuel, residual non-uniformities in the flat-field matrices, and systematic errors in the calibration procedure. Unfortunately, even the HPLC-grade *n*-heptane base fuel itself produces some LIF upon 248 nm illumination, and notably in the 320 nm band (see Fig. 8). Here, the base fuel may contribute from 2–7 % of the total fluorescent signal, depending on the operating point. The flat-field correction at opposite configuration is quite accurate because the toluene LIF signal is used to obtain the relative flat-fielding matrix. The camera response accounted for in the flat-field matrix is from almost the same wavelength range as in the actual spray measurements. All in all, the estimate of accuracy is not quantitative.

However, for the one-side configuration, the flat-field approach using the toluene LIF signal itself cannot be used because of the dichroic beam splitter. Therefore, flat-field images are obtained using a white light source.

Fig. 15 Single shot LIF image of a heptane spray in the optical engine. The *red square* represents the selected area of the spray to determine the intensity decrease as function of the amount of flushed high-purity heptane
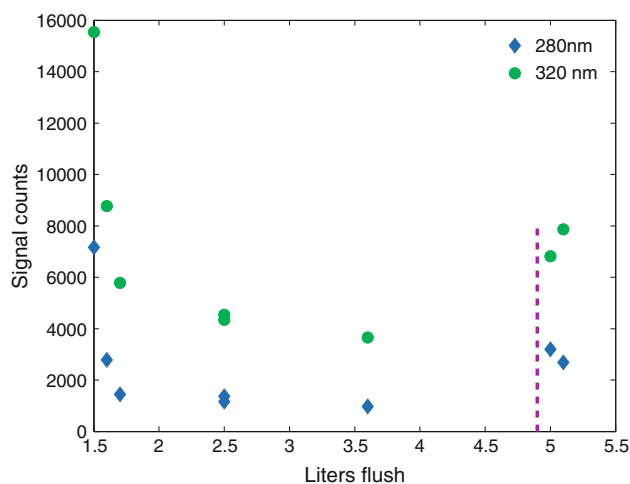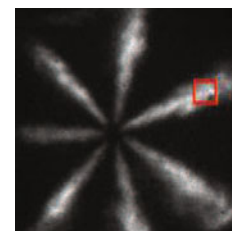

Fig. 16 Intensity as function of pure *n*-heptane flush. The fueling system was filled with 99.3 % pure *n*-heptane prior to flushing with 99.6 % pure *n*-heptane. Images are recorded at −20 CAD ATDC, (laser power 60 mJ, camera gain = 100). The *vertical line* separates different measurement days. The counts are not accumulated

5 Results

The results section is split into two major parts. Part one presents the results in the optically accessible engine, the second part presents the result in the high-pressure cell.

5.1 Optically accessible engine results

5.1.1 Residual fuel fluorescence

A basic assumption of the LIF ratio method is that the fluorescence transmitted by the bandpass filters is really due only to the tracer. Thus, it is imperative that the fuel itself does not fluoresce upon 248 nm irradiation. Before each measurement series, we check for fluorescence signal during fuel injection without adding toluene to the system. Initial experiments were performed with spectrometric-grade n-heptane (99.3 % pure). This has always resulted in clearly recognizable spray images (Fig. 15), obviously due to fluorescence of trace components in the fuel. The whole fuel line was then flushed with HPLC-grade n-heptane (99.6 % stated purity; Sigma-Aldrich) without recirculating the fuel back to the tank. Figure 16 shows the time evolution of the average signal in one of the spray tips (location indicated in Fig. 15) measured on both cameras, as a function of the amount of fuel flushed through the fuel line (including fuel pump, tubing and injector). After an initial fast decrease, the signal gradually decreases further, but not to zero, especially on the 320 nm camera. After having the system stay idle overnight, the fluorescence was again increased (data points to the right of the vertical dashed line), apparently due to residuals in crevices in the fueling system that leaked back into the fresh fuel.
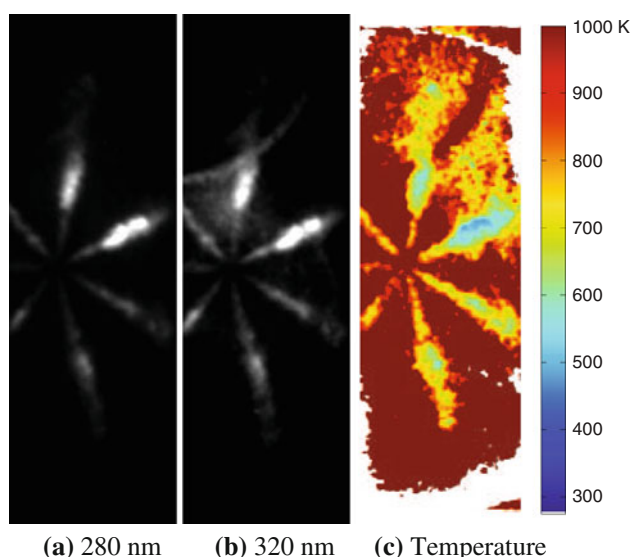

(a) 280 nm   **(b)** 320 nm   **(c)** Temperature

Fig. 17 Fuel injection in nitrogen with toluene recorded at 20 CAD before TDC. Injection started 25 CAD before TDC

This residual fluorescence may give rise to LIF ratios that deviate strongly from those expected for toluene fluorescence at the same temperature. Therefore, during actual toluene LIF measurements, the signal must be sufficiently high for the residual contribution to be negligible.

5.1.2 Temperature during fuel injection

Temperature stratification during fuel injection was investigated by adding toluene to the inlet manifold. Together with air, the toluene will be entrained by the injected fuel spray, which should allow visualization of the temperature field in and around the sprays. A representative result of the measurements, and a translation of the LIF ratios to a temperature field on the basis of Fig. 14, is shown in Fig. 17 (non-reactive conditions). The recorded images are smoothed by 12 × 12 neighbor averaging, thus achieving a lateral resolution comparable to the thickness of the excitation laser light sheet. Pixel values below 300 counts (after background subtraction) are discarded.

The temperature field, although qualitatively correct, shows a number of artifacts. Some of these are due to the mechanical construction of the combustion chamber (the valve seats are clearly visible), some others likely relate to multiple scattering or fluorescence trapping by the sprays. The global temperature field is uniform, but shows a LIF ratio-based temperature that is approximately 250 K above the global temperature derived from the pressure trace. The high ratios at the valve edge and in between the sprays suggest trapping of fluorescent signal which is more pronounced in the 280 nm region than in the 320 nm region. The cold fuel spray regions are clearly recognizable.

5.2 High-pressure cell results

To investigate the spray temperature field in more detail than is possible in an engine environment, experiments have been conducted in a high-pressure cell. The purpose of the research is to investigate the major characteristics of the temperature distribution, while a spray propagates into hot ambient gas. The experimental conditions are listed in Table 5.

We present two separate data sets. The first one is obtained by a same side camera configuration and the second by an opposite side arrangement. The laser sheet thickness converges from 1.8 to 0.8 mm from left to right

Table 5 Experimental conditions of spray injection

Injection pressure	900 bar
Injection duration	2 ms
Ambient temperature	590 K
Ambient density	20 kg/m^3

in the HPC, and therefore, the spatial resolution at the laser entrance side will be lower than at the far end. The spray enters the cell diagonally at the far end, see Fig. 3.

5.2.1 Temperature distribution in the spray region

Same side camera configuration results The results presented in this section are for the same side camera configuration. The obtained spatial scaling factor is 9.28 pixels/mm. The images are smoothed by 12×12 neighbor averaging, to represent the same spatial resolution as the average laser sheet thickness in the middle of the HPC (1.3 mm). The fuel doped with 10 vol.% toluene is injected into ambient conditions of $T_{amb} = 590$ K, for a duration of 2 ms. Per injection one image is acquired, the delay time is advanced in steps of 0.5 ms to investigate the time evolution. As a result, each pair of images originates from separate injections.

As mentioned above, the dichroic beam splitter is suspected to affect the temperature calibration of the LIF ratio, because its optical characteristics vary with angle of incidence of the incoming light. Evidence for this is presented in Fig. 18. Panel (a) shows the fluorescence intensity (integrated over part of the laser light sheet width in (c)) as a function of laser penetration depth into the HPC. (Zero corresponds to where the laser beam enters the field of view.) This measurement was made about 2 s after fuel/

toluene injection into the HPC, after which time the mixing fan is expected to have homogenized the cell contents. Obviously, the signals drop with increasing penetration depth. In itself, this could simply be due to absorption of the laser beam. Figure 18d, however, shows that also the LIF ratio drops with increasing penetration depth, in spite of the presumably uniform temperature. This effect is found to be independent on incident laser power and of toluene concentration; we attribute it to the beam splitter. Note that, according to the curves of Fig. 4, it is indeed the "red" part of the spectrum that is most sensitive to the exact switching wavelength of the beam splitter.

Using Fig. 18d as a correction curve, the temperature distributions of the sprays are calculated, as shown in Fig. 19. The fuel is injected out of the top right corner and the laser beam propagates from left to right as indicated in Fig. 3. The rectangle in Fig. 19 indicates the extent of the laser light sheet. It does not directly illuminate the liquid part of the spray; for our conditions, the liquid length of the spray is estimated to be 27 mm using a mixing-limited spray vaporization model [19]. Other areas may be excited indirectly by laser scattering via the walls or by multiple scattering.

Increased background levels due to undesired fluorescence contribute to the systematic errors of the LIF ratio which result in a temperature of approximately 19 % above the ambient temperature. To account for these systematic

Fig. 18 a, **b** Camera intensities for both wavelength regimes (**c**) 280 and 320 nm part of the fluorescence signal after spray injection and homogenization as function of the distance from the *left side* of the field of view (**d**) mean value and standard deviation of 13 vertically averaged scaled ratio curves. The ratio is scaled using the average ratio in *x*-direction
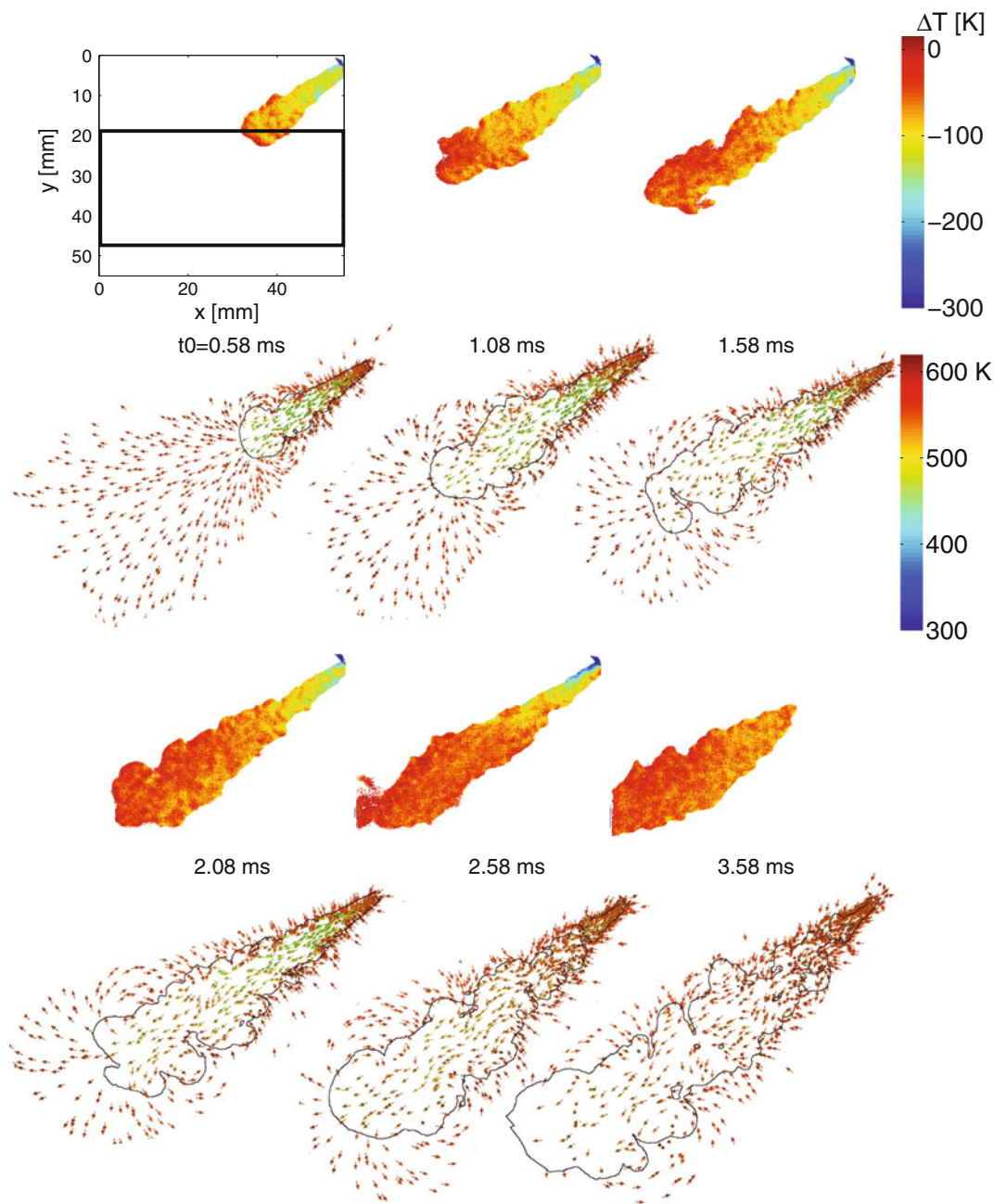

(a) 320 nm

(b) 280 nm

(c) 280 nm and 320 nm

(d) Scaled ratio curves
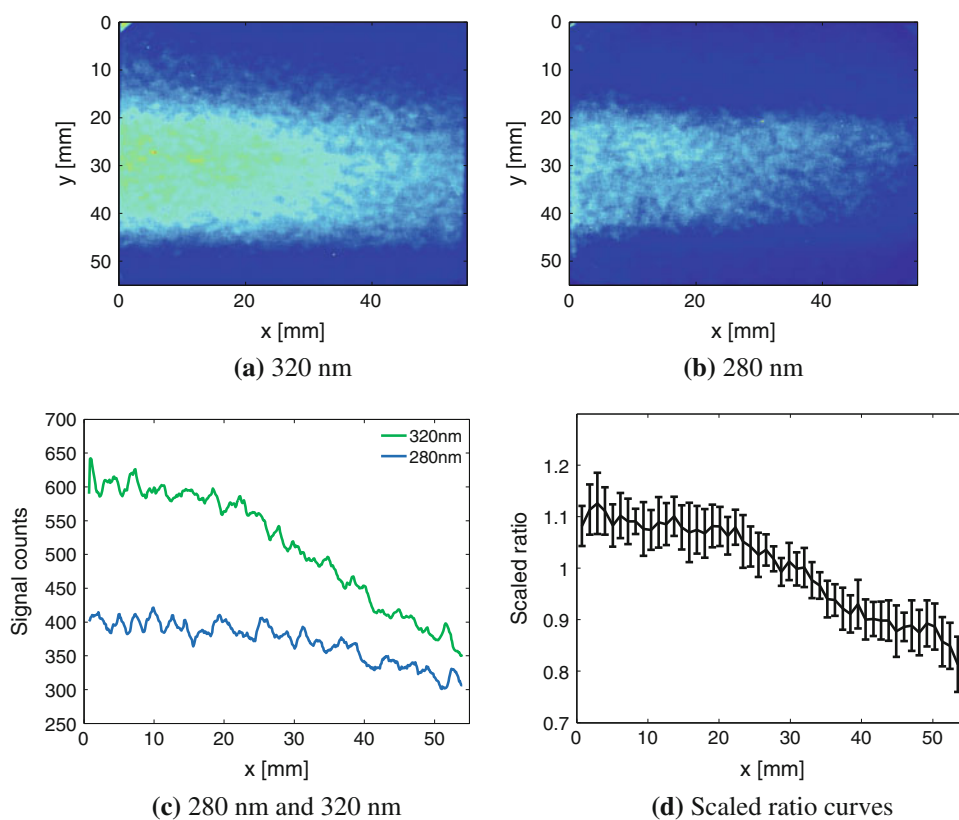
Fig. 19 Comparison between temperature distribution in the HPC, given as a temperature difference between the ambient temperature and velocity fields obtained with LES. The *black rectangle* in the *top left image* represents the laser sheet area. Toluene *outside this rectangle* is excited by multiple scattering. The velocity vectors are *colored* according to temperature. The limited field of view of the experimental setup prohibits visualization of the complete spray at 2.58 and 3.58 ms. The *solid black line* in the LES defines where the mass fraction of the fuel is $Y_{fuel}= 0.001$

errors, the edge of the spray is assumed to have the same temperature as the ambient gas and the other temperatures are given as a temperature difference with respect to this boundary temperature.

When observing the experimental spray development in a two-dimensional cross section, one can conclude that the temperature field coincides with the simplified and generally accepted view of a diverging spray due to air entrainment, which should result in heating of the fuel from the core region outwards and in downstream direction. However, at the 1.58 and 2.08 ms point, large cusps in the spray pattern might indicate increased air entrainment and therefore increased temperatures in these cusps compared to other nearby regions. The experimental results are compared with LES (described in Appendix A) to verify the findings.
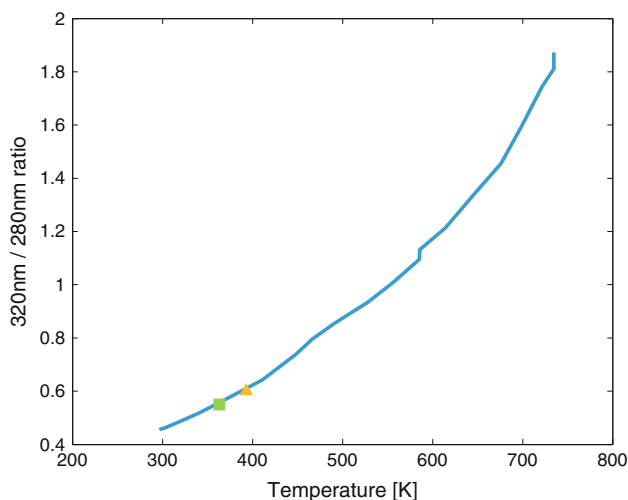
Fig. 20 Temperature calibration line for the opposite-camera configuration. The *square* and *triangle* represent two measurement points from toluene vapor ratios at known ambient temperature

5.2.2 Opposite camera configuration results

The opposite side camera setup obviously is not plagued by beam splitter artifacts. We have determined independent calibration points for the LIF signal ratio by evaporating toluene into the heated HPC. These results will be compared to the IFPEN-based calibration curve here.

The temperature calibration line in Fig. 20 is obtained using the same approach as in Sect. 4. It differs from the one presented in Fig. 14 because of the lack of the dichroic beam splitter. The image also presents two data points obtained from toluene vapor at two different ambient temperatures. As expected, the ratio calibration points match well with the IFPEN data and once again prove the validity of the calibration approach presented in Sect. 4.

6 Conclusions and recommendations

In principle, Planar Toluene LIF is capable of visualizing temperature distributions with high precision, instantaneously, and with good spatial resolution.

The working principle being based on the intensity ratio between fluorescence in two disjunct wavelength bands, the toluene PLIF method is, however, susceptible to a number of potential pitfalls, several of which have been discussed in this paper. These are of two kinds. On the one hand, the signal intensity drops quickly with rising temperature, giving rise to increased uncertainty. From this point of view, it may be worthwhile to study the possible effect that saturation may have on the fluorescence spectrum; should this be negligible, then the method would be safe to use in the saturated regime, which is beneficial for the signal level.

On the other hand, there is the issue of fluorescence wavelength selection. Modern coating techniques can produce bandpass filters that combine a narrow transmission wavelength band with steep edges and high ($\sim$90 %) transmission efficiency, but these spectral properties depend on the angle of light incidence. The desire to collect as much light as possible, and thus using fast collection optics, then introduces variations in the spectral collection efficiency over the field of view. This translates into a spatial dependence of the calibration factor. We have found such effects for the dielectrically coated optics used in our "same-side" configuration (Fig. 7a). Similar issues, at least with the same net effect of location-dependent deviation in the spectral collection efficiency, may arise if measurements are performed close to reflecting surfaces.

We have discussed two ways to obtain calibration data, based on either accurate spectra measured at IFPEN, or LIF signal ratios in our own setups at known, independently measured temperatures, both methods show good agreement. Temperature field measurements in and around fuel sprays have been evaluated, and show a precision of about 4 %. Comparison with LES shows similar hot regions and gradients. The accuracy of the experimental temperature fields, however, is negatively effected by residual fluorescence of the base fuel (HPLC-grade *n*-heptane). As in all measurements through spectral bandpass filters, the actual spectral information in the signal is lost, and one must assume that all light transmitted by the filter really originated from the molecules of interest. To avoid that assumption, a spectrograph can be used, but this obviously goes at the expense of at least one spatial dimension.

Appendix A: Comparison with LES

The LES code used in this study is the fully compressible AVBP solver co-developed by IFP Energies Nouvelles and CERFACS for structured and unstructured meshes [20]. The second order centred Lax–Wendroff convective scheme [21] is combined with an explicit time advancement. Unresolved subgrid-scale turbulence is modeled by a Smagorinsky model [22] with constant coefficient. The dispersed liquid phase is resolved using a mesoscopic Eulerian formalism [23]. The region close to the injector, dominated by high volumetric ratios of liquid fuel and

breakup effects, is not included in the simulations. The DIturBC injector model [24] is used to bridge that region by imposing physical flow conditions at a distance approximately 10 nozzle diameters downstream of the injector outflow plane. Its principle is to impose boundary conditions for the two phase flow at a distance downstream of the injector nozzle, in regions where the flow has been dispersed by breakup phenomena and can be addressed by a diluted mesoscopic Eulerian formalism.

The LES has been run on a computational mesh which represents a closed combustion vessel with slightly larger dimensions than the HPC (112^3 versus 108^3 mm^3). It consists of a tetrahedral mesh with local refinement. The mesh size near the nozzle exit is 80 μm and gradually increases to 800 μm toward the other end of the domain, yielding approximately 0.7 million nodes and 4.3 million cells. All boundaries, except for the injection plane, are taken as adiabatic walls which have negligible influence on the spray internal structure. This mesh has been chosen on the basis of spray formation results presented in [25].

The simulated spray penetration is compared to the measured one. The fuel vapor penetration in the LES is taken at the point in space where the mass fraction of the fuel is $Y_{fuel} = 0.001$, as defined in the first Engine Combustion Network workshop [26]. For the experiments, the vapor edge is clearly visible and determined visually. The spray penetration length of a single LES and one experiment are shown in Fig. 21. The first measured point in time ($t_0 = 0.58$ ms) is fixed on the LES penetration. Subsequently, this is taken as a reference for all other measured points. The error bar of the point at 2.08 ms is defined from the minimum and maximum values from the 9 measurements. Figure 21 shows a good agreement between the experiments and the LES.

The results of the LES are also given in Fig. 19; velocity vectors are colored with the corresponding temperature at that point. Furthermore, the contour of the fuel spray ($Y_{fuel} = 0.001$) is indicated with the solid black line. The LES results reveal heavy mixing in a pulsating fashion due
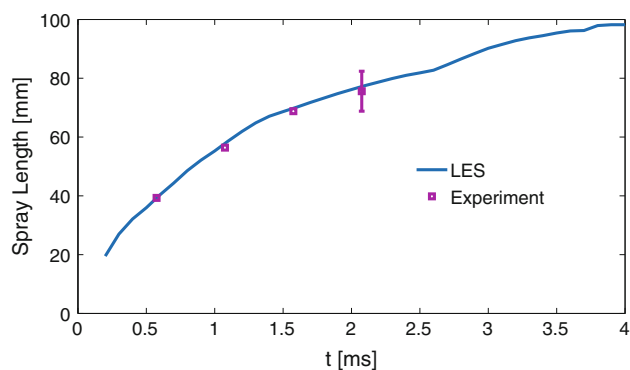
to spray-induced vortices at the edge, resulting in hot spots of ambient air enclosed in the spray core region. The LES predicts temperatures in the order of 500 K for the inner spray areas, whereas the experimental results are much closer to the ambient condition of 590 K. Possible reasons might be the averaging effect in the experiment due to the laser thickness.

Appendix B: Data processing

The complete data processing procedure includes removing background, spatial alignment, flat-field correction, ratio calculation and converting to temperature distribution. Suppose we obtain an image pair, of which $I_r(x, y)$ is the pixel intensity of the "red" part of the spectrum (320 nm) at position x, y and $I_b(x, y)$ is the pixel intensity of the "blue" part of the spectrum (280 nm). In the case of a one-side configuration, the data correction procedure for both images can be expressed as:

$$I_{r,corr}(x, y) = (I_r(x, y) - B_r(x, y))\, TR(x, y)\, F_r(x, y) \tag{1}$$

and

$$I_{b,corr}(x, y) = (I_b(x, y) - B_b(x, y))\, F_b(x, y), \tag{2}$$

where $B(x, y)$ is the background signal, $TR(x, y)$ the spatial transformation matrix and $F(x, y)$ is the flat-field matrix. In case of opposite configuration, the data processing procedure can be expressed as:

$$I_{r,corr}(x, y) = (I_r(x, y) - B_r(x, y))\, TR(x, y)\, C_r(x, y) \tag{3}$$

and

$$I_{b,corr}(x, y) = (I_b(x, y) - B_b(x, y)), \tag{4}$$

where the major difference is the relative flat-fielding matrix $C_r(x, y)$. To only present temperature regions, which have reasonable accuracy, pixels with less than 300 counts are neglected because of the low signal-to-noise ratio. The temperature distribution can be obtained with the calibration relation.

$$T(x, y) = T(R(x, y)) = T\left(\frac{I_{r,2}(x, y)}{I_{b,2}(x, y)}\right) BS\,(x, y), \tag{5}$$

where $R(x, y)$ is the LIF ratio distribution and $BS(x, y)$ is the correction for the beam splitter, which is only used in one-side configuration of the HPC experiments.

Fig. 21 Spray length as function of injection time

References

1. R. Devillers, G. Bruneaux, C. Schulz, Appl. Phys. B Lasers Opt. **96**, 735–739 (2009). doi:10.1007/s00340-009-3563-3
2. C. Schulz, V. Sick, Prog. Energy Combust. Sci. **31**(1), 75–121 (2005)

3. G. Tea, G. Bruneaux, J. Kashdan, C. Schulz, Proc. Combust. Inst. **33**(1), 783–790 (2011)
4. W. Koban, J.D. Koch, R.K. Hanson, C. Schulz, Phys. Chem. Chem. Phys. **6**, 2940–2945 (2004)
5. K. Mohri, M. Luong, G. Vanhove, T. Dreier, C. Schulz, Appl. Phys. B Lasers Opt. **103**, 707–715 (2011). doi:10.1007/s00340-011-4564-6
6. W. Koban, J. Koch, R. Hanson, C. Schulz, Appl. Phys. B Lasers Opt. **80**, 147–150 (2005). doi:10.1007/s00340-004-1715-z.
7. F.P. Zimmermann, W. Koban, C.M. Roth, D.-P. Herten, C. Schulz, Chem. Phys. Lett. **426**(46), 248–251 (2006)
8. M. Luong, R. Zhang, C. Schulz, V. Sick, Appl. Phys. B Lasers Opt. **91**, 669–675 (2008). doi: 10.1007/s00340-008-2995-5
9. J. Mannekutla, A. van Vliet, R. Klein-Douwel, N. Dam, H. ter Meulen, *in* European Combustion meeting (2011)
10. E. Doosje, Limits of mixture dilution in gas engines. PhD thesis, Eindhoven University of Technology, 2010
11. R.S.G. Baert, P.J.M. Frijters, B. Somers, C.C.M. Luijten, W. de Boer, SAE Technical Paper 2009-01-0649 (2009)
12. S. Krüger, G. Grünefeld, Appl. Phys. B Lasers Opt. **69**, 509–512 (1999). doi: 10.1007/s003400050844
13. M. Luong, W. Koban, C. Schulz, J. Phys. Conf. Ser. **45**(1), 133 (2006)
14. J. Lindén, C. Knappe, M. Richter, M. Aldén, Meas. Sci. Technol. **23**(3), 035201 (2012)
15. Semrock (2012), http://www.semrock.com/filter-spectra-at-non-normal-angles-of-incidence.aspx
16. W. Koban, J.D. Koch, R.K. Hanson, Schulz C, Appl. Phys. B Lasers Opt. **80**, 777–784 (2005). doi:10.1007/s00340-005-1769-6
17. T.C. Williams, C.R. Shaddix, Rev. Sci. Instrum. **78**(12), 123702 (2007)
18. U. Egüz, L. Somers, C. Leermakers, L.D. Goey, Int. J. Veh. Des. **55**(1), 76–90 (2011)
19. J. Pastor, J. López, J. García, J. Pastor, Fuel **87**, 2871–2885 (2008)
20. V. Moureau, G. Lartigue, Y. Sommerer, C. Angelberger, O. Colin, T. Poinsot, J. Comput. Phys. **202**(2), 710–736 (2005)
21. P. Lax, B. Wendroff, Commun. Pure Appl. Math. **13**, 217–237 (1960)
22. J. Smagorinsky, Mon. Weather Rev. **91**(3), 99–164 (1963)
23. P. Février, O. Simonin, K.D. Squires, J. Fluid Mech. **533**, 1–46 (2005)
24. L. Martinez, A. Benkenida, B. Cuenot, Fuel **89**, 219–228 (2010)
25. C. Bekdemir, L. Somers, L. de Goey, J. Tillou, C. Angelberger, Proc. Combust. Inst. **34**(2), 3067–3074 (2013)
26. E. Hawkes, *in* ECN1 workshop (2011), http://www.sandia.gov/ecn/